Characteristic Modes Analysis of Non-Uniform Metasurface Superstrate for Nanosatellite Antenna Design

FRANCESCO ALESSIO DICANDIA, (Member, IEEE), AND
SIMONE GENOVESI, (Senior Member, IEEE)
Dipartimento di Ingegneria dell'Informazione, University of Pisa, 56122 Pisa, Italy

Corresponding author: Simone Genovesi (simone.genovesi@unipi.it)

ABSTRACT This work addresses the use of the Characteristic Modes Analysis (CMA) for tailoring a Metasurface (MTS) in view of exploiting it in compact, low-profile, Circularly Polarized (CP) antennas. The investigated non-uniform MTS is exploited as a superstrate in the design of a novel compact and low-profile antenna for nanosatellite applications. The MTS consists of a 3×4 array of unequal patches arranged in a rectangular lattice. The antenna parameters are carefully tailored by using the CMA to achieve a significant performance enhancement with respect to a uniform MTS in terms of both Axial Ratio (AR) bandwidth and aperture efficiency. The reliability of the CMA approach is verified by assessing the overall performance of the whole radiating structure comprising the stripline feeding excitation. The proposed MTS antenna is compact ($0.068 \lambda 0$) provides a remarkable aperture efficiency going from 86 % up to 96 % and an AR coverage in the upper hemisphere greater than 84 % within the desired S-band (2.025 – 2.29 GHz).

INDEX TERMS Characteristic modes, cubeSat, S-band, circular polarization, metasurface.

I. INTRODUCTION

In the last few years satellite communication systems have undergone a significant growth with the purpose of providing a reliable connection to as many users as possible in the worldwide, even in remote regions [1]. In particular, nanosatellites are becoming increasingly important into the space market due to the shorter manufacturing time as well as a lower cost of production [2]. Nanosatellites are easier to customize for satisfying the broad range of applications such as earth observation, meteorology, internet of things and deep space [3], [4]. Among all the components on this kind of platforms, the radiating elements are of paramount importance in providing the desired communication system performance and efficiency, which has an obvious impact on the satellite life. Indeed, they allow the exchange of telemetry, tracking and control (TTC) information useful for monitoring the attitude and provide the necessary payload data transfer. Over the past years, several examples of CubeSat antennas have been proposed [5], [6]. For instance, an aperture-coupled microstrip line-fed patch antenna array with circular polarization was introduced in [7] where the C-band radiator exploits

the deployable wings for becoming fully operative. In [8] an aperture coupled S-band CubeSat antenna was obtained by using three Wilkinson power dividers in order to provide four signals with an appropriate phase difference. An array of four rectangular patches in the S-band (2.4 - 2.45G Hz) has been proposed in [9]. A stacked patch with an air gap between the two patch radiators was shown in [10]. Several other examples are also illustrated in [3], [11] that confirm the amount of continuous efforts done for searching for better solutions.

In the last years, an electromagnetic analysis based on resonant modes, the Characteristic Modes Theory (CMT) [12], [13], has proved to be an helpful approach for inspiring innovative designs in MIMO systems [14], pattern reconfigurable antennas [15], [16] and for antennas mounted on three dimensional platforms [17]–[22]. Basically, CMT provides a set of orthogonal current modes (J_n) that the considered structure is able to support. These resonant modes solely depend on the platform shape and dimensions, regardless of any external feeding arrangement. Suitable non-resonant exciters must be placed on the object to stimulate the proper current modes to transform the platform itself into an efficient radiator [19]. The benefits of exploiting the CMT on complex platforms have been recently highlighted in [23] where a

compact radiating system comprising four subwavelength exciters placed on the edges of a 1U-CubeSat face is capable of providing both beam steering capability and polarization agility within the amateur S-band (2.4 - 2.45 GHz). Moreover, CMT has been employed to study the radiation properties of finite Metasurfaces (MTSs) of few unit cells [24]. MTSs are bidimensional arrangements of periodic elements that exhibit useful electromagnetic properties for enhancing the radiation performance of antennas [25], [26]. Some examples of MTS antennas designed by using the CMT are also reported in [27]–[32]. More in detail, MTS antenna solutions able to radiate a linearly polarized (LP) electric field are proposed in [27], [28], [32] whereas MTS radiators with a CP field are shown in [29]–[31].

The purpose of this article is to illustrate the use of the CMT for tailoring a MTS in view of exploiting it in compact, low-profile, Circularly Polarized (CP) antennas. The proposed methodology is adopted for the design of an antenna with a MTS superstrate suitable to be mounted on a single face of a 1U CubeSat platform ($10 \times 10 \times 10$ cm^3) and operating in the whole Earth Exploration Satellite Services (EESS) frequency band (2025 - 2290 MHz) adopted for telemetry/payload downlink as well as telecommand uplink. The proposed antenna is composed of a non-uniform MTS superstrate layer excited by stripline through a rectangular slot. Differently from previous non-uniform MTS layers [28], [33], the proposed MTS consists of a non-uniform rectangular patches only along y axis direction whose dimensions are tapered following a Chebyshev distribution (Fig. 1). For both dimensions the gap among the patches is constant (W_s). The CMT is able to provide useful physical insights by looking at current distributions excited on the MTSs and then avoids an approach based on brute force parametric full-wave optimizations. More in detail, the rectangular slot behaves like an inductive exciter [34] capable of stimulating on the metasurface layer two orthogonal CMs whose

Characteristic Angles (CAs) differ 90° on average within the considered bandwidth and hence can radiate a CP field. The antenna achieves a good impedance matching within the whole requested frequency range, a remarkable maximum gain and a noteworthy Axial Ratio (AR) angular coverage in the upper hemisphere. The paper is organized as follows. In Section II, the Characteristic Mode Analysis (CMA) of the proposed non-uniform MTS superstrate is addressed. In particular, the effects of a finite solid Ground Plane (GP) and that of a slotted one have been carefully addressed. The following Section III is devoted to the CP performance enhancement ensured by the proposed non-uniform MTS and to the comparison with a uniform MTS. Finally, the full-wave antenna analysis is addressed in Section IV whereas conclusions are drawn in Section V.

II. CMA OF THE METASURFACE SUPERSTRATE

The modal analysis of the investigated structure provides a set of orthogonal current modes (J_n) that can be used to express the total current distribution (J_{tot}) through a weighted linear combination of them:

$$J_{tot} = \sum_n a_n J_n \tag{1}$$

where the complex coefficient a_n represents the modal excitation degree related to each current mode (J_n), also known as Modal Weighting Coefficient (MWC). The inspection of the current modes (J_n) distributions and their correspondent far fields provide guidelines to control the radiation performance of the examined object by a proper tune of the MTS. The following sections will focus on finding the most appropriate current modes that have to be excited.

A. INFINITE GROUND PLANE

The final geometry of the proposed MTS layer consists of non-uniform rectangular patches arranged in a 3×4 array configuration (Fig. 1). The rectangular patches array are printed on the top face of a grounded dielectric layer (Rogers TMM3, $\varepsilon_r = 3.46$, $\delta = 0.002$) with a thickness of $h_1 = 6.985$ mm. Differently from the non-periodic MTS structure consisting of adjustable square-ring patches proposed in [28], the addressed structure presents a non-uniform arrangement only along y axis direction. In particular, a Chebyshev length tapering with a sidelobe attenuation of 12 dB was applied to the rectangular patches largest side ($Lpxi$, $i = 1, 2$). A rectangular shape MTS unit cell ($ratio_i = Wpyi/Lpxi$, $i = 1, 2$) has been adopted in order to facilitate the achievement of 90° phase difference between two orthogonal electric field components. The reason of adopting a non-periodic MTS instead of a uniform rectangular lattice will be explained in the next section. All the optimized geometric parameters are reported in the caption of Fig. 1.

In the CMA one of the most important parameters is represented by the CA, α_n [35], defined as:
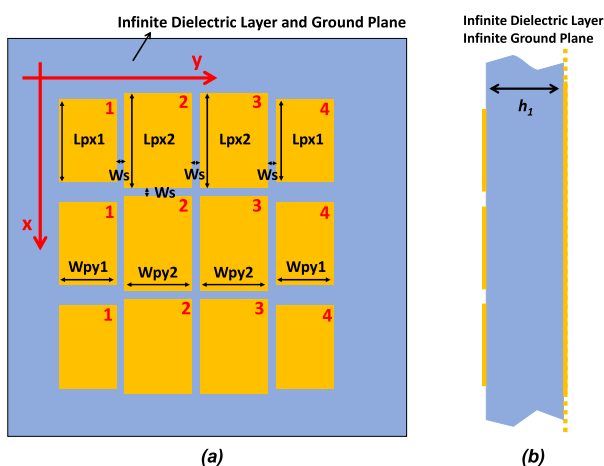
$$\alpha_n = 180° - \tan^{-1}(\lambda_n) \tag{2}$$

FIGURE 1. (a) Top view and (b) side view of the proposed metasurface superstrate layer with infinite dielectric layer and ground plane. $Lp \times 1 = 28.95$ mm, $Lp \times 2 = 30.8$ mm, $Ws = 2.55$ mm, $ratio_1 = 0.72$, $ratio_2 = 0.68$ and $h_1 = 6.985$ mm.

where λ_n represents the eigenvalue of the nth CM. The CA characterizes the phase difference between the current mode (J_n) and the related electric field mode (E_n) [36]. At first, to take into account solely the effect of 3×4 non-uniform upper rectangular patches array, the grounded dielectric layer has been considered infinitely extended. All the CMA have been performed by using the full-wave solver FEKO [37]. The CA of the first ten modes as a function of the frequency is reported in Fig. 2.
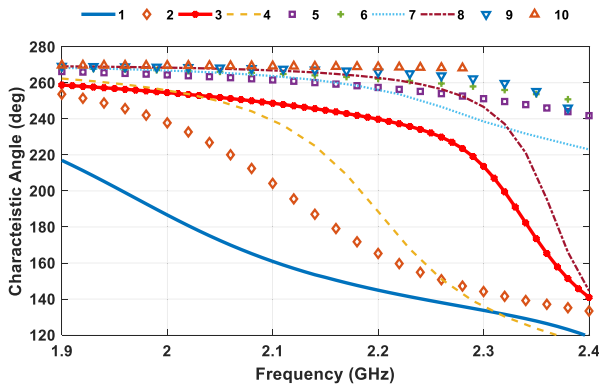
FIGURE 2. CA as a function of the frequency of the first ten CMs in case of infinite grounded dielectric layer.

From the CA behaviour, it is apparent that at low frequencies only *Mode 1* is near the resonance (CA = 180°). However, with the increasing of the frequency, more and more CMs approach the resonance and so they start to provide a significant contribution to the radiation if properly excited. It is worth noting that, to achieve a CP radiation field in far field region two orthogonal electric field components with equal amplitude and a phase difference of 90° are needed. Among all the CMs supported by the investigated structure, only *Mode 1*, *Mode 3*, *Mode 6*, *Mode 8*, *Mode 9* and *Mode 10* present a broadside ($\theta = 0°$) radiation pattern (Fig. 3).

The surface current modes distribution (J_n) on the MTS and the related 3D normalized radiation patterns of each broadside CM evaluated at 2.15 GHz are illustrated in Fig. 4 and Fig. 5, respectively. *Mode 1* exhibits a surface current distribution mainly along x axis (Fig. 4a) whereas *Mode 3* (Fig. 4b) presents a similar distribution but primarily polarized along y axis. The other current modes are characterized by different orientations on the rectangular patches, which causes a less focused radiation pattern than *Mode 1* and *Mode 3* (Fig. 5). However, the broadside direction of the field radiated by a characteristic current is not enough to guarantee the CP. It is also necessary to verify that the two modes have comparable orthogonal electric field components (E_θ, E_ϕ). For this reason, the electric field components of the first ten modes along broadside direction ($\theta = 0°$) is depicted in Fig. 6.

Fig. 6 confirms that *Mode 2*, *Mode 4*, *Mode 5* and *Mode 7* are characterized by a radiation pattern null along broadside direction ($\theta = 0°$) as highlighted in Fig. 3, whereas the couples *Mode 1* and *Mode 3* or *Mode 8* and *Mode 10* generate two
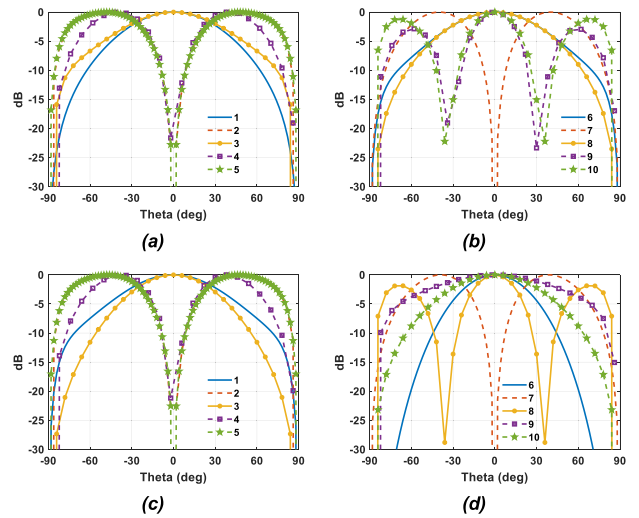

FIGURE 3. Normalized modal radiation patterns in the principal planes at 2.15 GHz; (a) modes 1–5 $\phi = 0°$ plane, (b) modes 6–10 $\phi = 0°$ plane, (c) modes 1–5 $\phi = 90°$ plane and (d) modes 6–10 $\phi = 90°$ plane.
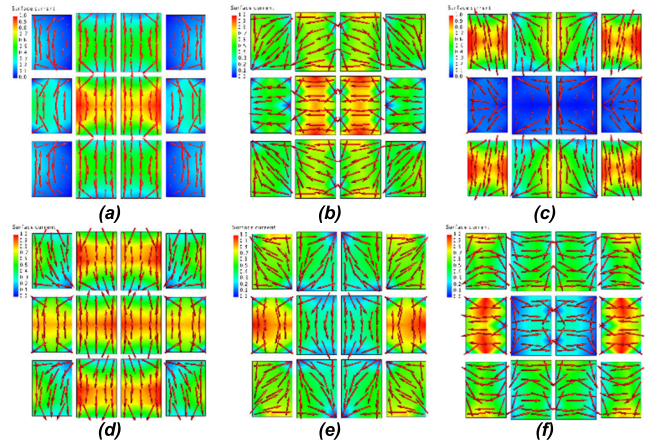

FIGURE 4. Normalized current mode distribution (J_n) on the metasurface layer evaluated at 2.15 GHz; (a) Mode 1, (b) Mode 3, (c) Mode 6, (d) Mode 8, (e) Mode 9 and (f) Mode 10.
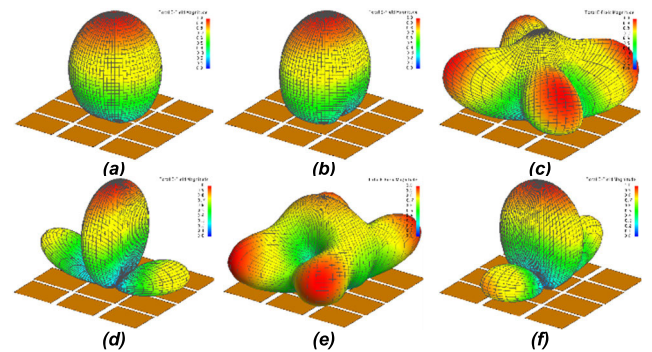

FIGURE 5. Normalized 3D modes radiation pattern evaluated at 2.15 GHz; (a) Mode 1, (b) Mode 3, (c) Mode 6, (d) Mode 8, (e) Mode 9 and (f) Mode 10.

similar orthogonal electric field components (E_θ, E_ϕ) toward broadside. By analysing both the CA of Fig. 2 and the radiated electric field pattern mode of Fig. 6 it is possible to conclude
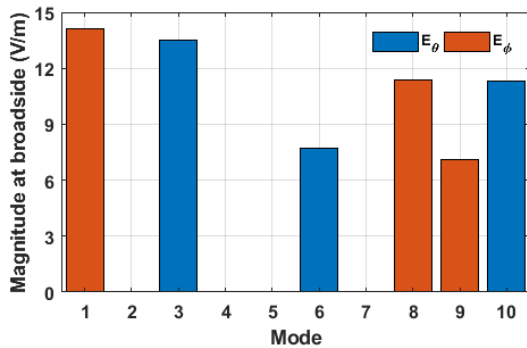
FIGURE 6. Electric field mode components along broadside direction ($\theta = 0°$) at 2.15 GHz.

FIGURE 8. Normalized current mode distribution (J_n) on the MTS layer related to *Mode 1* and *Mode 3* within the desired EESS band; (a) *Mode 1* at 2.025 GHz, (b) *Mode 1* at 2.15 GHz, (c) *Mode 1* at 2.29 GHz, (d) *Mode 3* at 2.025 GHz, (e) *Mode 3* at 2.15 GHz and (f) *Mode 3* at 2.29 GHz.

that the best CMs pair to be efficiently stimulated on the investigated non-uniform MTS is represented by *Mode 1* and *Mode 3* since they present similar orthogonal electric field amplitude as well as a CA with a relative phase difference close to 90° within the desired frequency band.

To better highlight the latter condition, the CA phase difference with respect to *Mode 1* is calculated and reported in Fig. 7 where it is well visible that *Mode 3* and *Mode 1* have a phase difference between 75° to 95° within the addressed frequency band (2025 - 2290 MHz).
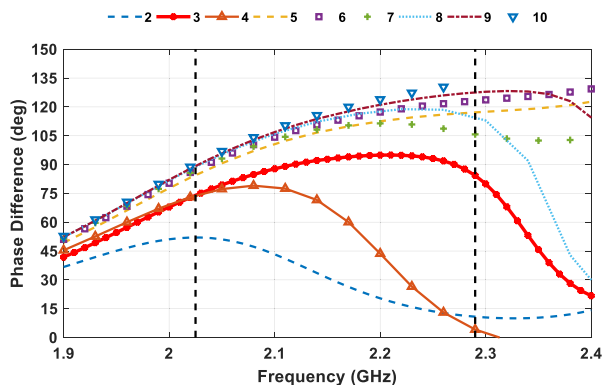

FIGURE 7. CA phase difference with respect to *Mode 1* as a function of the frequency in case of infinite grounded dielectric layer.

Since the CMA depends on the frequency [12], [14], the evolution of the modal current distribution (J_n) related to the identified CMs pair (*Mode 1* and *Mode 3*) within whole EESS frequency band (2025 - 2290 MHz) is reported in Fig. 8. As expected, the current modes undergo a gradual variation as a function of the frequency. More in detail, *Mode 3* current intensity in the middle of the MTS (Fig 8*d-e-f*) fades little by little with the increasing of frequency whereas it becomes stronger and stronger at the corners. Instead, *Mode 1* presents a more stable current distribution with respect the frequency. However, even if a slight surface current alteration occurs with respect to the frequency the associated radiation pattern maintains a maximum radiation field toward broadside radiation ($\theta = 0°$).

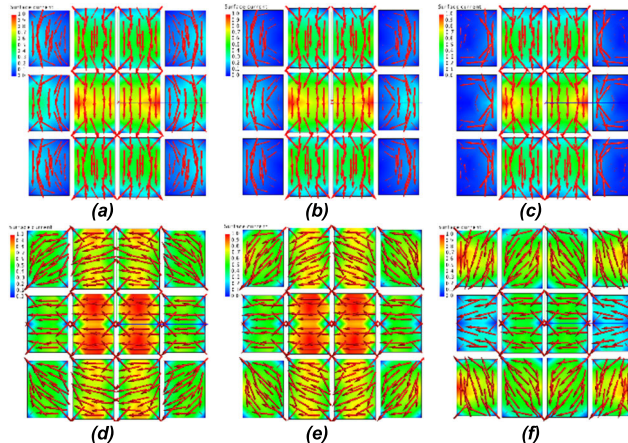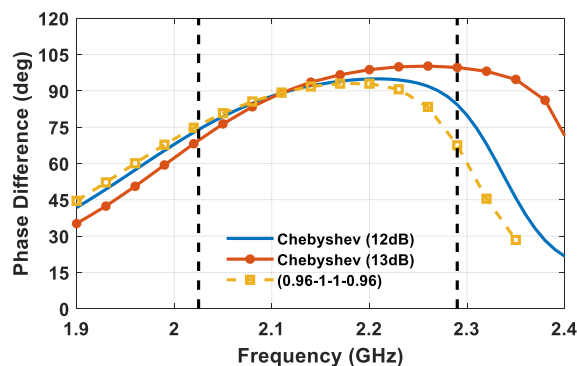**FIGURE 9.** CA phase difference with respect to *Mode 1* as a function of the frequency in case of infinite grounded dielectric layer.

The CA phase difference between *Mode 1* and *Mode 3* in case of different length tapering as a function of the frequency is reported in Fig. 9 to motivate the adoption of a Chebyshev length tapering with a sidelobe attenuation of 12 dB for the patches longer side ($Lpxi$, $i = 1, 2$).

In particular, the Chebyshev length tapering with a sidelobe attenuation of 13 dB and a smaller non-uniform MTS condition with a normalized length of $Lpx1 = 0.96$ and $Lpx2 = 1$ have been reported for comparison. The alteration of the CA phase difference in case of different taperings is due mainly to the variation of *Mode 3* CA behavior with respect to the frequency. From Fig. 9 it is clear that the selected length tapering, namely Chebyshev with a sidelobe attenuation of 12 dB, represents the best condition that guarantees the smallest distance to the desired CA phase difference of 90° within the desired bandwidth between the selected modes.

B. FINITE GROUND PLANE WITH A RECTANGULAR SLOT

In the previous subsection, the CMA of a non-uniform MTS superstrate layer with both the substrate and an infinite GP has been carried out. In particular, a pair of orthogonal modes

(*Mode 1* and *Mode 3*) has been identified as efficient modes in order to provide a CP field. However, differently from the previous MTS antennas designed by the CMT [29]–[31], in this subsection the effect of a finite square GP of the dimension of the 1U CubeSat face (*i.e.* $L = 100$ mm) will be examined. Moreover, the beneficial effect of the presence of a rectangular slot etched on the finite GP will be illustrated as well. Furthermore, as in previous works on MTS antennas [28]–[32], an infinite dielectric layer has been considered for the CMA.

The sketch of the proposed metasurface layer composed by an array of 3×4 non uniform rectangular patches, a finite square GP and a rectangular slot with dimension of $Lslot = 52$ mm, $Wslot = 3.5$ mm is depicted in Fig. 10. The CAs of the *Mode 1* and *Mode 3* of the described MTS (Fig. 10) with respect to the frequency are shown in Fig. 11. In particular, the comparison by considering an infinite grounded dielectric layer (*Infinite* GP), an infinite dielectric substrate Rogers TMM3 with thickness h_1 but finite GP (*Finite GP*) and the effect of a rectangular slot etched on the finite GP (*Finite GP+Slot*) have been taken into account. As it is apparent,
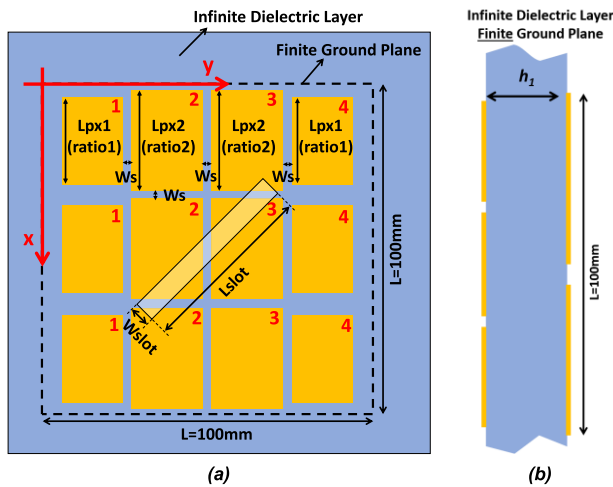
the finiteness of the GP introduces a significant alteration of the CA trend. In fact, it is evident a decreasing of the curves slope, especially for *Mode 1*. In particular, *Mode 1* undergoes a considerable reduction of the CA value at frequencies lower than 2.05 GHz whereas the CA increases for frequency above 2.05 GHz with respect to the case of infinite GP. *Mode 3* presents similar behaviour but with a more pronounced CA difference between 2.3 - 2.4 GHz. The introduction of the rectangular slot rotated of 45° on the finite GP provides a further modification of the CA behaviour. Specifically, a downshift of the CA value related to *Mode 1* can be observed whereas *Mode 3* presents a slight rise of the CA value up to 2.2 GHz with respect to Finite GP case.

A comprehensive view of the differences among the three analysed cases is provided by Fig. 12 where the phase difference between *Mode 1* and *Mode 3* is reported. It can be seen that even if the array of 3×4 non-uniform rectangular patches located on the top side of the MTS exhibits a relative phase difference between the modes close to 90° around 2.15 GHz (*Infinite GP* case), the presence of a finite GP significantly degrades the CA phase difference between the two orthogonal CMs. In fact, within the desired frequency band the phase difference between CMs is around 60°. Therefore, the finite GP affects the CP field produced by the joint excitation of *Mode 1* and *Mode 3* because the currents excited on the square ground are not in the proper 90° out-of-phase condition. On the contrary, by etching a rectangular slot rotated of 45° on the finite GP, a rigid upshifts of the CA phase difference by keeping similar curve slope is obtained. The slot dimensions ($Lslot = 52$ mm, $Wslot = 3.5$ mm) have been optimized in order to roughly maintain this 90° phase displacement between the CA related to *Mode 1* and *Mode 3* within the desired bandwidth.

FIGURE 10. (a) Top view and (b) side view of the proposed metasurface superstrate layer by considering the finite ground plane with a rectangular slot.
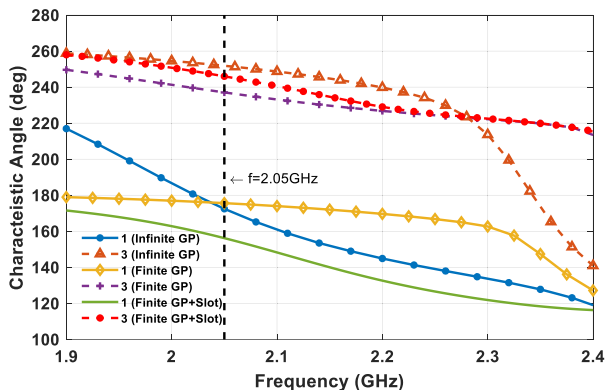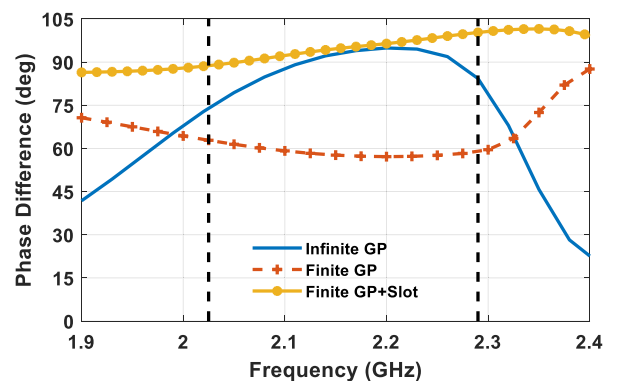

FIGURE 11. CA comparison as a function of the frequency of the two desired CMs (*Mode 1* and *Mode 3*).

FIGURE 12. Characteristic Angle (CA) phase difference comparison between *Mode1* and *Mode 3* as a function of the frequency.

A rectangular slot rotated of 45° etched on the finite GP can be exploited as inductive exciter to provide the necessary 90° CA phase difference between *Mode 1* and *Mode 3*. In fact, the slot is capable of stimulating efficiently on the metasurface layer the CMs characterized by a maximum of the current nearby the exciter, hence the desired *Mode 1* and

Mode 3, due to their maximum current in the middle of the MTS (Fig. 4*a-b*).

In addition, to prove that the *Finite GP+Slot* case does not corrupt the *Mode 1* and *Mode 3* current distribution on the non-uniform MTS (Fig. 4*a-b*), the correlation coefficient (ρ) has been calculated by considering the modal radiation pattern of the MTS in case of *Infinite GP* and *Finite GP+Slot* (Table 1) [16], [38]. From Table 1 it is possible to assert that, due to the very high correlation value, the presence of a finite GP and the slanted rectangular slot does not corrupt the modal current distribution on the non-uniform MTS, but mainly alter the CA trend as a function of the frequency (Fig. 11).

TABLE 1. *Mode 1* and *Mode 3* Correlation between *Infinite GP* and *Finite GP+Slot*.

Frequency (GHz)	*Mode 1*	*Mode 3*
2.025	0.94	0.92
2.15	0.92	0.9
2.29	0.91	0.89

Finally, the performance in term of the expected AR at broadside direction are calculated under the assumption that only *Mode 1* and *Mode 3* are equally stimulated on the MTS (Fig. 13). The reported estimated ARs highlight not only the importance of considering all the components of the antenna and their finite extension for a reliable design but also the better results achieved with respect to consider an infinite GP. In fact, even if in case of an infinite GP the antenna is not able to provide an AR lower than 3 dB within whole the desired S-band, when the finite GP structure and the rectangular slot are simultaneously taken into account, the AR performance drastically improves and an AR lower than 3 dB is guaranteed within the S-band. This beneficial effect is due to a better CA phase difference between the orthogonal *Mode 1* and *Mode 3* (Fig. 12) whereas the poor AR value in case of finite GP (without the rectangular slot) is due to a CA phase difference around 60°.
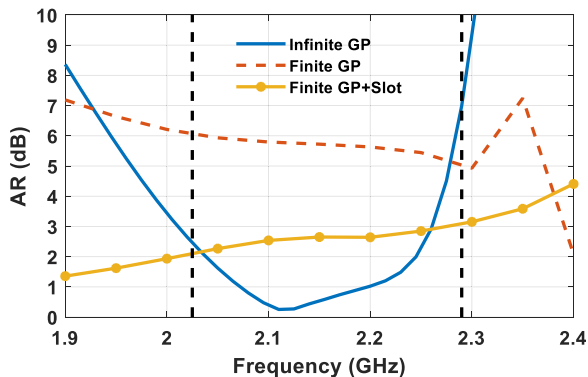
FIGURE 13. Axial Ratio (AR) at broadside direction as a function of the frequency by stimulating only *Mode 1* and *Mode 3* on the metasurface.

III. UNIFORM VS NON-UNIFORM METASURFACE COMPARISON

In order to motivate the choice of a non-uniform arrangement only along *y* axis direction (1D non-uniform MTS), the CMA is used in this section to compare the CP performance of the proposed 1D non-uniform MTS with respect to a uniform one [39]. For a fair comparison, both structures have been considered printed on an infinite grounded dielectric layer (Rogers TMM3) with a thickness h_1. Moreover, the dimensions of the uniform rectangular patches printed on the top face of the dielectric substrate are optimized in order to overlap the CA of *Mode 1* of the two structures to better visualize the differences (Fig. 14*a*).
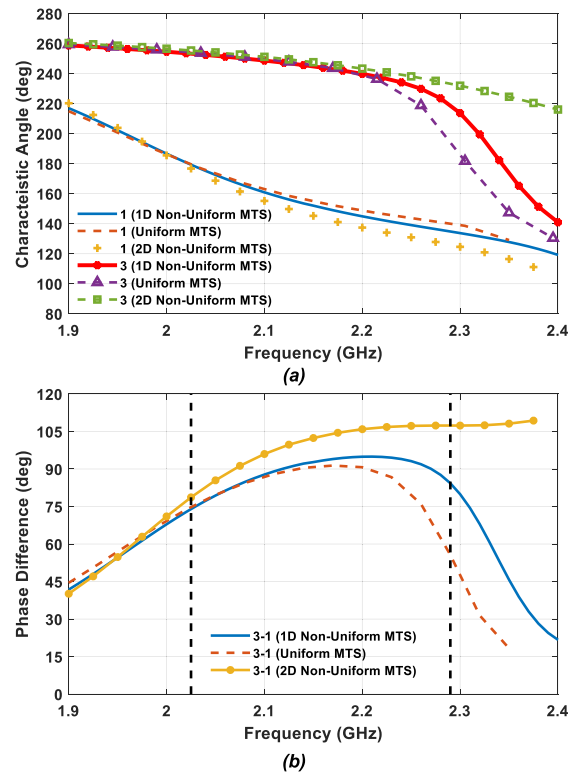
FIGURE 14. Comparison between the non-uniform and uniform MTS in terms of (a) CA related of *Mode 1* and *Mode 3* and (b) CA phase difference as a function of the frequency in case of infinite grounded dielectric layer.

From Fig. 14*a* it is clear that *Mode 3* of 1D non-uniform MTS and uniform MTS shows a dissimilar trend above 2.2 GHz. In fact, the 1D non-uniform MTS allows obtaining higher CA value related to *Mode 3* from 2.2 GHz that ensures an improvement of the bandwidth within which a 90° phase difference is kept between this pair of modes (Fig. 14*b*). The CA related to *Mode 1* and *Mode 3* in case of a bidimensional non-uniform MTS (2D non-uniform MTS) by using the Chebyshev length tapering with a sidelobe attenuation of 12 dB for both the coordinate (*x-y* axis) is also reported in Fig. 14 to further highlight the beneficial effect of a non-uniform rectangular patch arrangement only along the *y* axis direction. For a fair comparison, the dimensions of the 2D non-uniform MTS rectangular patches are optimized

to overlap the CA of *Mode 1* and then to compare the performance with the same *Mode 1* resonance frequency with respect to the other solutions. Fig. 14*a* underlines that the 2D non-uniform MTS significantly increases *Mode 3* resonance frequency whereas *Mode 1* CA remains almost unchanged. These trends turn out to be detrimental for the CP radiation since the CA phase difference between the two identified CMs moves away from the 90° condition within the considered bandwidth (Fig. 14*b*).

The downshift of the *Mode 3* resonance frequency with a consequent reduction of the *Mode 3* CA behavior as a function of the frequency can be a possible solution in case of 2D non-uniform MTS to achieve in average 90° phase difference over a larger bandwidth. However, this solution needs larger dimensions of the MTS and this is not compatible to the size of a single face of a 1U CubeSat platform and also reduces the antenna aperture efficiency.

The trend of the CA phase difference in case of 1D non-uniform MTS affects positively the AR at broadside direction as a function of the frequency. Indeed, from Fig. 15, it can be seen that the 1D non-uniform MTS outperforms the uniform one since an improvement of the AR percentage bandwidth from 9.5% (uniform MTS) to 12.5% (non-uniform MTS) is achieved by exploiting the non-uniform MTS arrangement. Moreover, even if the 2D non-uniform MTS allows improving the AR bandwidth (10.8 %) with respect to the uniform one (9.5 %), its performance remains worse than the proposed 1D non-uniform MTS.
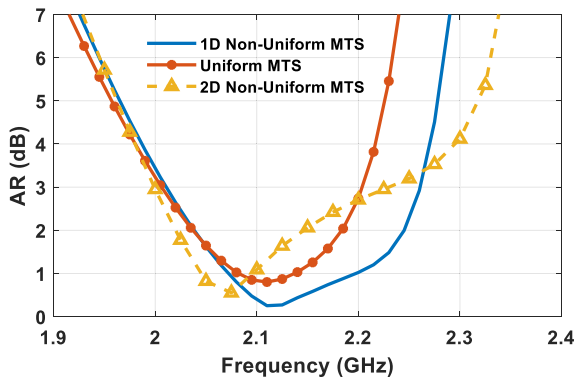

FIGURE 15. Axial Ratio (AR) comparison at broadside direction between non-uniform and uniform MTS as a function of the frequency by equally stimulating only *Mode 1* and *Mode 3* in case of infinite grounded dielectric layer.

In addition to the AR improvement, the 1D non-uniform arrangement also offers a higher maximum gain at broadside direction as a function of the frequency than uniform MTS, especially for frequencies above 2.1 GHz as highlighted in Fig. 16. Finally, the gain at broadside ($\theta = 0°$) as a function of the frequency further confirms the superior performance of the 1D non-uniform MTS along *y* direction with respect to the 2D non-uniform MTS. Indeed, a gain reduction of around 0.6 dB from 2 GHz to 2.2 GHz is achieved in case of 2D non-uniform MTS. The 2D non-uniform MTS is
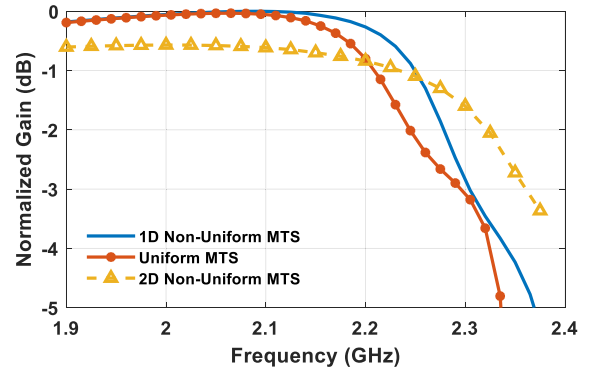

FIGURE 16. Normalized gain at broadside comparison between non-uniform and uniform MTS as a function of the frequency by equally stimulating only *Mode 1* and *Mode 3* in case of infinite grounded dielectric layer.

characterized by a higher gain for frequencies above 2.25 GHz but with a poor CP radiation since its AR is greater than 3 dB (Fig. 15).

As stated before, the previous analysis has been carried out by considering the MTS on an infinite grounded dielectric layer, but the same trend is obviously retained when the exciter is considered.

IV. CP S-BAND ANTENNA WITH A NON-UNIFORM METASURFACE SUPERSTRATE

The previous CMA provided the necessary guidelines for designing a MTS for a S-band antenna mountable on a 1U CubeSat platform. The lateral and top view of the antenna is shown in Fig. 17. The proposed antenna is compact and low profile ($0.068 \lambda_{0@2.15 GHz}$) and comprises four metallic layers and four dielectric substrates. More in detail, *Substrate#1* (Rogers TMM3, $\varepsilon_r = 3.46$, $\delta = 0.002$) has been employed to print the non-uniform MTS (*Layer#1*). *Substrate #2* and *Substrate#4* are made of Rogers TMM4 laminate with a thickness $h_2 = 0.508$ mm and $h_4 = 1.905$ mm, respectively. *Substrate#3* is Rogers RO4450B and it is employed to attach the two TMM4 laminates together. The two conductive layers, *Layer#2* and *Layer#4* are the ground reference for the asymmetric stripline feeder that is located on *Layer#3*. Moreover, *Layer#2* behaves also as the ground plane for the non-uniform MTS. The rectangular slot is etched on the GP of the MTS (*Layer#2*) and it is rotated by 45° for exciting the desired *Mode 1* and *Mode 3* on the MTS through its magnetic current distribution, as well as to provide the 90° phase difference between *Mode 1* and *Mode 3* (Fig. 12). In order to avoid the propagation of the parallel plate mode in the asymmetric stripline feeding, six metallic vias have been placed around the slot [40]. The distance between the slot and the metallic vias has been optimized by considering both the impedance matching and the maximum antenna gain. Besides, a SMA coaxial cable on the back side is used to feed the antenna (Fig. 17). It is worth noting that differently from the previous designed CP MTS antenna [29]–[31], [39], the adopted stripline feeding
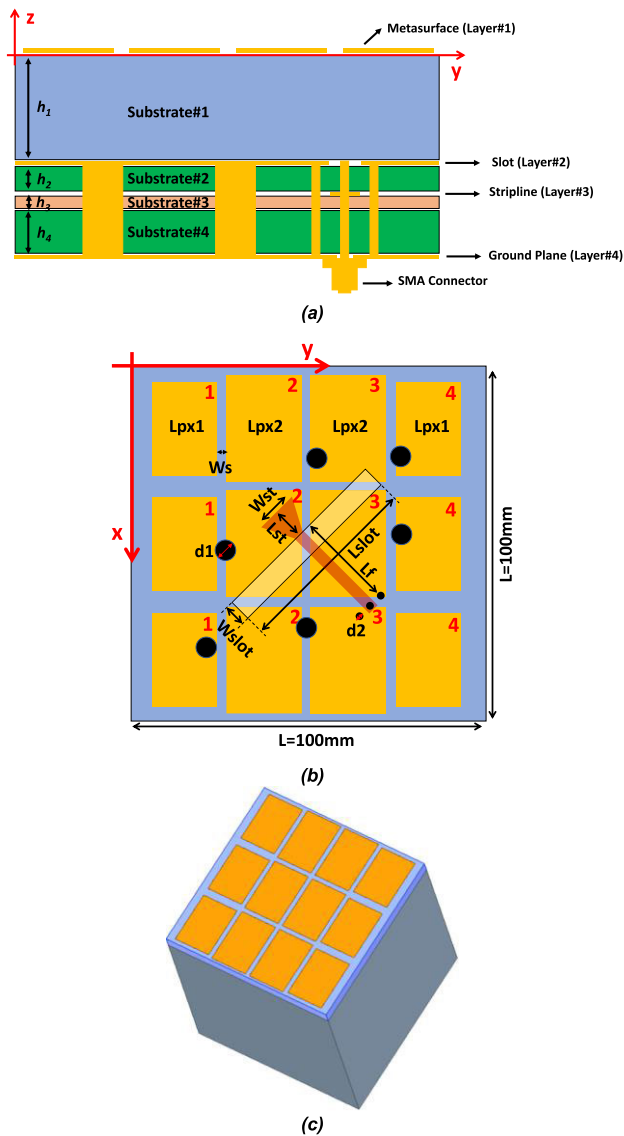
FIGURE 17. (a) Side view, (b) top view and (c) mounted-on-platform view of the proposed CubeSat antenna.

FIGURE 18. Simulated S_{11} as a function of the frequency.
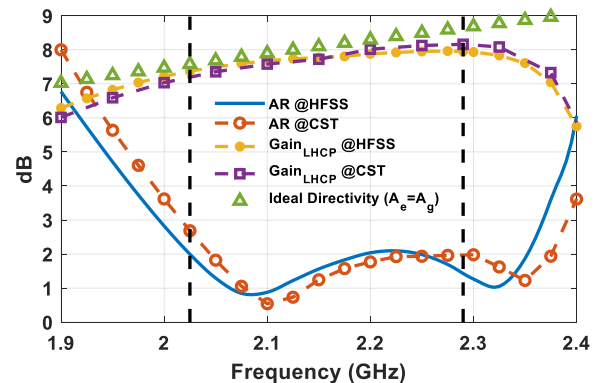
FIGURE 19. Simulated gain value at broadside direction ($\theta = 0°$) and AR with respect to the frequency.

technique make the antenna performance more robust to the interference with other components, devices and the host platform due to the presence of the ground below the stripline that isolate the antenna.

A comparison between the S_{11} parameter with and without the MTS is shown in Fig. 18 where it is possible to appreciate the good performance within EESS frequency band (2.025 - 2.29 GHz) where values lower than -10 dB from 1.98 GHz to 2.34 GHz (16.67 %) can be observed. Furthermore, two other resonances are visible around 1.75 GHz and 2.55 GHz. The gain left-hand CP (Gain $_{LHCP}$) at broadside direction ($\theta = 0°$) along with the AR are displayed in Fig. 19. The ideal directivity of an aperture with the same dimensions of the single CubeSat face (10×10 cm^2) has been reported as well to consider the case of an antenna with an effective area (A_e) equal to the geometrical area (A_g). Good agreement
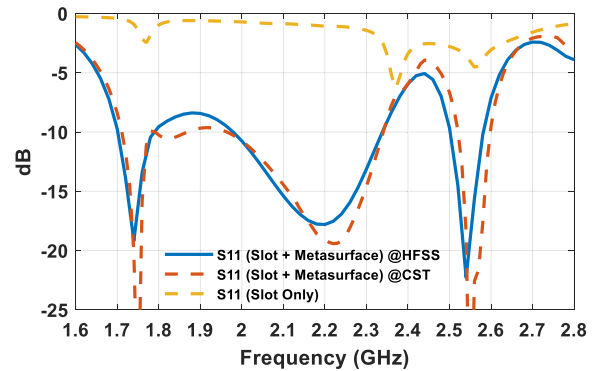
is apparent between results obtained by using HFSS from Ansys Electronic Suite and CST Microwave Studio.

The MTS antenna is characterized by a considerable aperture efficiency since its value remains close to 96 % from 1.9 GHz up to 2.1 GHz, with a gain spanning from 7.4 dBic at 2.025 GHz to 7.7 dBic at 2.1 GHz, and retain a significant aperture efficiency value of 86 % with a gain of 8 dBic at 2.29 GHz. From Fig. 19 it is also clear that the proposed antenna presents an AR lower than 3 dB from 1.99 - 2.37 GHz (17.43 %) and that within the desired working frequency the AR remains below 2 dB. The differences between the obtained AR with respect to the estimated AR by using the CMA (Fig. 13) will be addressed later.

The AR coverage as a function of the θ angle for both the principal planes ($\phi = 0°$, $\phi = 90°$) is presented in Fig. 20. As it is evident, at 2.025 GHz the AR remains below 3 dB for all θ angles of the principal planes whereas with the increasing of the frequency the AR angular coverage diminishes. However, to have a comprehensive overview about the AR angular coverage, all the upper hemisphere has to be considered. For this reason, the directions along which the radiated field exhibits an AR $\leq$ 3 dB have been calculated together with the correspondent gain within the Half Power Beamwidth (HPBW). As example, the performance of three frequencies (2.025 GHz, 2.15 GHz and 2.29 GHz)
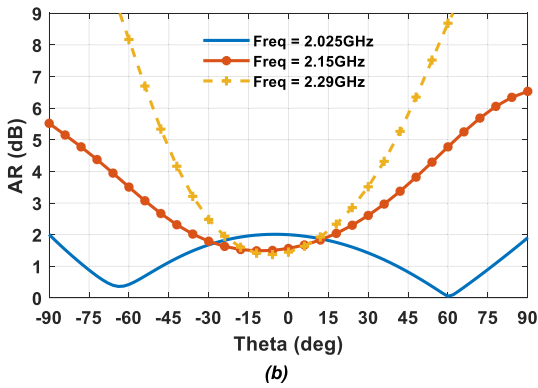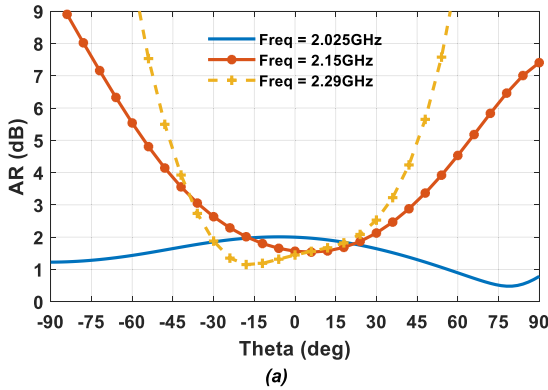
FIGURE 20. Simulated AR as a function of the θ angle for different frequency; (a) $\phi = 0°$, (b) $\phi = 90°$.
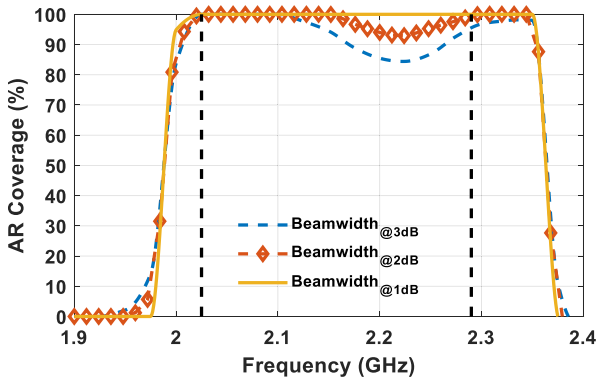

FIGURE 21. Percentage AR coverage as a function of the frequency for different beamwidth.

are mapped in Fig. 22 where three ranges of AR value are highlighted with different colors. These maps further emphasize that the proposed antenna provides a remarkable angular coverage in terms of HPBW and AR as a function of the frequency. Indeed, for the most angles (θ, ϕ) in the HPBW the AR turns out to be lower than 3 dB.

The performance of the proposed antenna are summarized in Table 2 and compared with those of solutions exploiting metasurfaces in terms of 3 dB AR bandwidth (ARBW), gain within the ARBW and the related percentage aperture efficiency. It is apparent that the described novel radiator outperforms the others in two of the three considered parameters.

TABLE 2. Performance comparison with other CP MTS antenna.

CP MTS Antenna	3 dB ARBW (%)	Gain (dBic)	Aperture Efficiency (%)
[29]	31.3	3.5-7	19-74
[30]	8.5	6.4-6.57	95-108
[31]	14.3	7-8.5	18-30
[41]	28.3	5.2-7.4	20-46
[42]	13	8.2-9.5	77-90
Proposed Antenna	17.43	7.1-8	70-96

More in detail, CP MTS antenna reported in [30] is characterized by a higher aperture efficiency but with a considerably lower 3 dB ARBW as well as the antenna gain. [29], [41] provide wider 3 dB ARBW but with a much worse aperture efficiency and antenna gain whereas CP MTS antenna reported in [42] presents a similar aperture efficiency but with a narrower 3 dB ARBW (13 %).

It is worth noting that all the previous results were obtained by considering the CP MTS antenna mounted on the top face of a 1U CubeSat platform (Fig. 17c). However, it is interesting to observe that the radiation performance remain almost unchanged even for the antenna considered standalone since most of the current distribution is excited on the top face of the proposed non-uniform MTS and because the adopted feeding technique isolates the antenna from the rest of the platform. To prove this, the correlation coefficient (ρ) has been calculated by considering the radiation pattern in case of the standalone antenna and the antenna mounted on the top face of a 1U CubeSat platform (Table 3).

TABLE 3. Correlation between antenna standalone and antenna mounted on a top face of a 1U CubeSat.

Frequency (GHz)	2.025	2.15	2.29
ρ	0.98	0.97	0.95

The high correlation value as a function of the frequency performance assesses the similar performance of the two structures and further confirms the robustness of the proposed antenna with respect to the external platform as well as the CubeSat equipment.

A. AR STATISTICAL ANALYSIS

A statistical characterization of the designed MTS antenna has been also performed to further assess the MTS antenna performance. The percentage *AR coverage* has been defined as the number of the angles (θ, ϕ) where the AR exhibits a value lower than 3 dB over the total number of the angles (θ, ϕ) for which the gain is within the beamwidth and it is plotted Fig. 21. Three different beamwidths (3 dB, 2 dB and 1 dB) are considered.
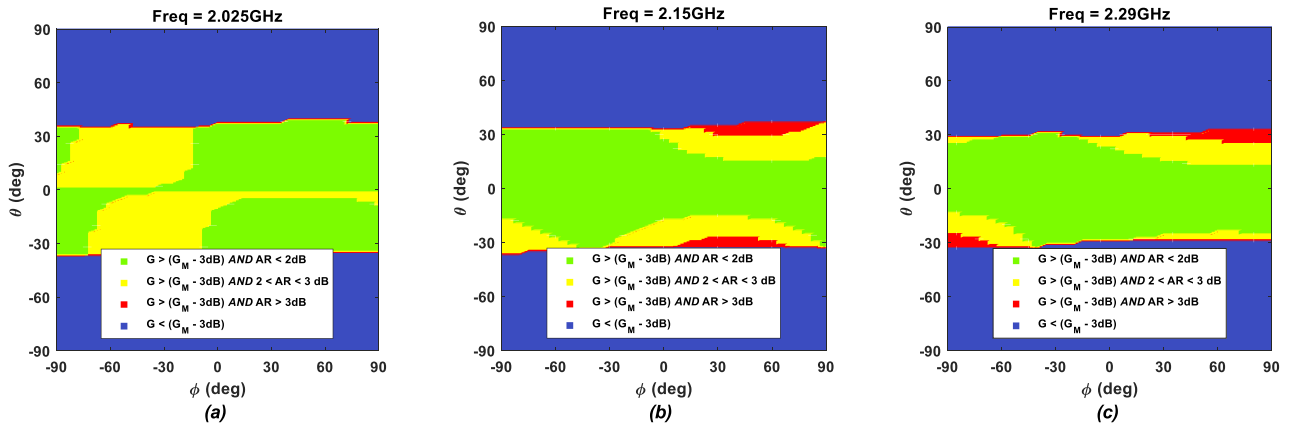
FIGURE 22. Color maps that highlight the direction along which the radiated field exhibits an AR ≤ 3 dB and a Gain (G) within the HPBW as a function of the frequency; (a) 2.025 GHz, (b) 2.15 GHz and (c) 2.29 GHz.

As it is evident from Fig. 21, within the desired frequency band the proposed antenna is able to provide always an AR below 3 dB (100% of AR coverage) in case of antenna beamwidth of 1 dB ($Beamwidth_{@1dB}$). However, by increasing the considered antenna beamwidth, a slight degradation of the *AR coverage* can be observed around 2.2 GHz that nevertheless ensures a value higher than 84 %.

In addition to the percentage *AR coverage*, the Cumulative distribution Function (C.d.F) of the AR is shown in Fig. 23. The color map of Fig. 23a highlights that the AR in the whole upper hemisphere presents a mean value (C.d.F = 0.5) lower than 3 dB within the frequency band 1.99 - 2.16 GHz with a minimum value of 1.44 dB at 2.075 GHz. Conversely, within the frequency range of 2.16 - 2.29 GHz the AR angular average in the upper hemisphere is included between 3 dB to 4.8 dB.

In order to have a comprehensive overview of the AR behavior, the C.d.F of the AR that take into account both the desired frequency band and the angles (θ, ϕ) into the whole upper hemisphere has been calculated and it is shown is Fig. 23b. The C.d.F of Fig. 23b emphasizes that the proposed antenna presents an comprehensive average value of the AR equal to 2.63 dB and a value larger than 3 dB in 45 % of cases.

B. MODAL EXCITATION COFFICIENT

In order to understand if the inductive excitation provided by the rectangular slot etched on the Layer#2 of the antenna (Fig. 17) is capable to efficiently excite the desired *Mode 1* and *Mode 3* identified from the previous CMA, the MWC (a_n parameter of the equation (1)) has been calculated. In particular, the correlation coefficient among CMs and the obtained radiation pattern [38], [43] has been exploited to retrieve the modal excitation degree. As it is apparent from Fig. 24, the MWC related to *Mode 1* and *Mode 3* is not constant as a function of the frequency but it is characterized by an opposite behaviour with respect to the frequency. In particular, *Mode 3* is more stimulated than *Mode 1* on
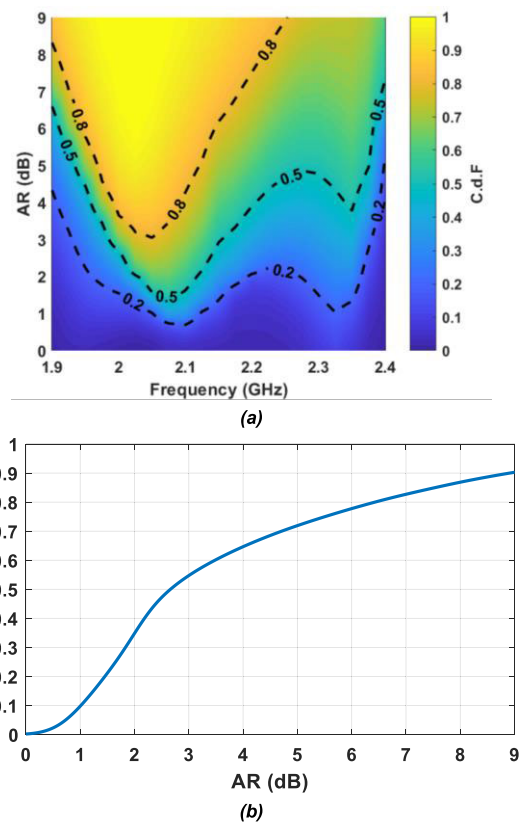

FIGURE 23. (a) C.d.F of the AR as a function of the frequency in the upper hemisphere and (b) C.d.F of the angular and frequency AR within the desired frequency.

the MTS layer at the lowest frequency. However, with the increasing of the frequency the *Mode 3* excitation goes down whereas the MWC of *Mode 1* increases more and more up to around 2.2 GHz where an exchange of the MWC trend occurs. Additionally, the inductive excitation achieved by the rectangular slot provides an equal modal excitation degree related to *Mode 1* and *Mode 3* on the MTS around 2.05 GHz and 2.35 GHz, responsible to the two peaks of the AR of Fig. 19.

Furthermore, the sum of the normalized power provided by *Mode 1* and *Mode 3* ($P_1 + P_3$) is always greater than 90 % within the desired S-band.

Therefore, it is confirmed that only *Mode 1* and *Mode 3* of the MTS are effectively stimulated since the other modes provide a normalized power less than the 10% of the total radiated power. It is worthwhile noting that the unequal MWC of Fig. 24 as a function of the frequency represents the main cause of a dissimilar AR behaviours between the attained AR of Fig. 19 and the calculated AR through the CMA of Fig. 13.
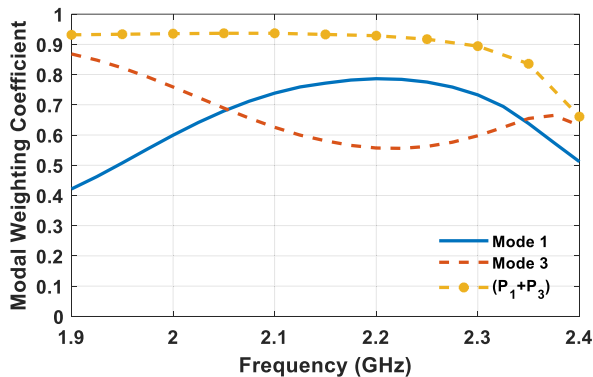

FIGURE 24. MWC and the normalized power provided by *Mode 1* and *Mode 3* with respect to the frequency.

V. CONCLUSION

The Characteristic Modes Analysis of a metasurface superstrate mounted on a finite structure has been carefully described. The effect of the non-uniform periodic surface, the finite size of the ground plane and the role played by the exciting slot have been highlighted by analysing the antenna performance. A compact and low-profile CP antenna compatible with a 1U CubeSat platform capable to cover the whole EESS frequency band (2025 - 2290 MHz) has been proposed as an example of the application of the described approach. The antenna exploits a non-uniform MTS that has been designed by recurring to the CMA for its tailoring. A thorough comparison with respect to a uniform MTS arrangement has been performed by resorting to the CMT. The results showed that the proper tailoring of the current modes of the non-uniform MTS allows improving the AR bandwidth and the aperture efficiency thus exhibiting a remarkable maximum gain at broadside direction.

Excellent performance in term of aperture efficiency and AR angular coverage over whole the desired S-band has been also confirmed by also taking into account the effect of the adopted feeding excitation scheme.

REFERENCES

[1] Y. Su, Y. Liu, Y. Zhou, J. Yuan, H. Cao, and J. Shi, "Broadband LEO satellite communications: Architectures and key technologies," *IEEE Wireless Commun.*, vol. 26, no. 2, pp. 55–61, Apr. 2019, doi: 10.1109/MWC.2019.1800299.

[2] M. N. Sweeting, "Modern small satellites-changing the economics of space," *Proc. IEEE*, vol. 106, no. 3, pp. 343–361, Mar. 2018, doi: 10.1109/JPROC.2018.2806218.

[3] N. Chahat, E. Decrossas, D. Gonzalez-Ovejero, O. Yurduseven, M. J. Radway, R. E. Hodges, P. Estabrook, J. D. Baker, D. J. Bell, T. A. Cwik, and G. Chattopadhyay, "Advanced CubeSat antennas for deep space and Earth science missions: A review," *IEEE Antennas Propag. Mag.*, vol. 61, no. 5, pp. 37–46, Oct. 2019, doi: 10.1109/MAP.2019.2932608.

[4] Z. Qu, G. Zhang, H. Cao, and J. Xie, "LEO satellite constellation for Internet of things," *IEEE Access*, vol. 5, pp. 18391–18401, 2017, doi: 10.1109/ACCESS.2017.2735988.

[5] S. K. Podilchak, A. P. Murdoch, and Y. M. M. Antar, "Compact, microstrip-based folded-shorted patches: PCB antennas for use on microsatellites.," *IEEE Antennas Propag. Mag.*, vol. 59, no. 2, pp. 88–95, Apr. 2017, doi: 10.1109/MAP.2017.2655581.

[6] G. Mishra, S. K. Sharma, and J.-C. S. Chieh, "A circular polarized feed horn with inbuilt polarizer for offset reflector antenna for *W*-band cubesat applications," *IEEE Trans. Antennas Propag.*, vol. 67, no. 3, pp. 1904–1909, Mar. 2019, doi: 10.1109/TAP.2018.2886704.

[7] P. Bouca, J. N. Matos, S. R. Cunha, and N. B. Carvalho, "Low-profile aperture-coupled patch antenna array for CubeSat applications," *IEEE Access*, vol. 8, pp. 20473–20479, 2020, doi: 10.1109/ACCESS.2020.2968060.

[8] M. J. Veljovic and A. K. Skrivervik, "Aperture-coupled low-profile wideband patch antennas for CubeSat," *IEEE Trans. Antennas Propag.*, vol. 67, no. 5, pp. 3439–3444, May 2019, doi: 10.1109/TAP.2019.2900428.

[9] A. Nascetti, E. Pittella, P. Teofilatto, and S. Pisa, "High-gain S-band patch antenna system for Earth-observation CubeSat satellites," *IEEE Antennas Wireless Propag. Lett.*, vol. 14, pp. 434–437, 2015, doi: 10.1109/LAWP.2014.2366791.

[10] P. Squadrito, P. Livreri, L. Di Donato, C. Squadrito, and G. Sorbello, "A telemetry, tracking, and command antennas system for small-satellite applications," *Electronics*, vol. 8, no. 6, p. 689, Jun. 2019, doi: 10.3390/electronics8060689.

[11] Y. Rahmat-Samii, V. Manohar, and J. M. Kovitz, "For satellites, think small, dream big: A review of recent antenna developments for CubeSats.," *IEEE Antennas Propag. Mag.*, vol. 59, no. 2, pp. 22–30, Apr. 2017, doi: 10.1109/MAP.2017.2655582.

[12] R. Harrington and J. Mautz, "Theory of characteristic modes for conducting bodies," *IEEE Trans. Antennas Propag.*, vol. 19, no. 5, pp. 622–628, Sep. 1971, doi: 10.1109/TAP.1971.1139999.

[13] Y. Chen and C.-F. Wang, *Characteristics Modes: Theory and Applications in Antenna Engineering*. Hoboken, NJ, USA: Wiley, 2015.

[14] D. Manteuffel and R. Martens, "Compact multimode multielement antenna for indoor UWB massive MIMO," *IEEE Trans. Antennas Propag.*, vol. 64, no. 7, pp. 2689–2697, Jul. 2016, doi: 10.1109/TAP.2537388.

[15] F. Dicandia, S. Genovesi, and A. Monorchio, "Null-steering antenna design using phase-shifted characteristic modes," *IEEE Trans. Antennas Propag.*, vol. 64, no. 7, pp. 2698–2706, Jul. 2016, doi: 10.1109/TAP.2016.2556700.

[16] F. A. Dicandia, S. Genovesi, and A. Monorchio, "Advantageous exploitation of characteristic modes analysis for the design of 3-D null-scanning antennas," *IEEE Trans. Antennas Propag.*, vol. 65, no. 8, pp. 3924–3934, Aug. 2017, doi: 10.1109/TAP.2017.2716402.

[17] M. R. Nikkhah, F. T. Dagefu, and N. Behdad, "Electrically small platform-based antennas for an unmanned ground vehicle," *IEEE Trans. Antennas Propag.*, vol. 68, no. 7, pp. 5189–5198, Jul. 2020, doi: 10.1109/TAP.2020.2977724.

[18] K. Ren, M. Ranjbar Nikkhah, and N. Behdad, "Design of dual-polarized, platform-based HF antennas using the characteristic mode theory," *IEEE Trans. Antennas Propag.*, vol. 68, no. 7, pp. 5130–5141, Jul. 2020, doi: 10.1109/TAP.2020.2975547.

[19] F. A. Dicandia, S. Genovesi, and A. Monorchio, "Efficient excitation of characteristic modes for radiation pattern control by using a novel balanced inductive coupling element," *IEEE Trans. Antennas Propag.*, vol. 66, no. 3, pp. 1102–1113, Mar. 2018, doi: 10.1109/TAP.2018.2790046.

[20] T.-Y. Shih and N. Behdad, "Bandwidth enhancement of platform-mounted HF antennas using the characteristic mode theory," *IEEE Trans. Antennas Propag.*, vol. 64, no. 7, pp. 2648–2659, Jul. 2016, doi: 10.1109/TAP.2016.2543778.

[21] Y. Chen and C.-F. Wang, "HF band shipboard antenna design using characteristic modes," *IEEE Trans. Antennas Propag.*, vol. 63, no. 3, pp. 1004–1013, Mar. 2015, doi: 10.1109/TAP.2015.2391288.

[22] Y. Chen and C.-F. Wang, "Electrically small UAV antenna design using characteristic modes," *IEEE Trans. Antennas Propag.*, vol. 62, no. 2, pp. 535–545, Feb. 2014, doi: 10.1109/TAP.2013.2289999.

[23] F. A. Dicandia and S. Genovesi, "A compact CubeSat antenna with beam-steering capability and polarization agility: Characteristic modes theory for breakthrough antenna design," *IEEE Antennas Propag. Mag.*, vol. 62, no. 4, pp. 82–93, Aug. 2020, doi: 10.1109/MAP.2020.2965015.

[24] F. H. Lin, T. Li, and Z. N. Chen, "Recent progress in metasurface antennas using characteristic mode analysis," in *Proc. 13th Eur. Conf. Antennas Propag. (EuCAP)*, Mar./Apr. 2019, pp. 1–5.

[25] J. Wang, Y. Li, Z. H. Jiang, T. Shi, M.-C. Tang, Z. Zhou, Z. N. Chen, and C.-W. Qiu, "Metantenna: When metasurface meets antenna again," *IEEE Trans. Antennas Propag.*, vol. 68, no. 3, pp. 1332–1347, Mar. 2020, doi: 10.1109/TAP.2020.2969246.

[26] M. Faenzi, G. Minatti, D. González-Ovejero, F. Caminita, E. Martini, C. Della Giovampaola, and S. Maci, "Metasurface antennas: New models, applications and realizations," *Sci. Rep.*, vol. 9, no. 1, p. 10178, Dec. 2019, doi: 10.1038/s41598-019-46522-z.

[27] T. Li and Z. N. Chen, "Wideband sidelobe-level reduced Ka-band metasurface antenna array fed by substrate-integrated gap waveguide using characteristic mode analysis," *IEEE Trans. Antennas Propag.*, vol. 68, no. 3, pp. 1356–1365, Mar. 2020, doi: 10.1109/TAP.2019.2943330.

[28] D. Chen, W. Yang, W. Che, and Q. Xue, "Broadband stable-gain multiresonance antenna using nonperiodic square-ring metasurface," *IEEE Antennas Wireless Propag. Lett.*, vol. 18, no. 8, pp. 1537–1541, Aug. 2019, doi: 10.1109/LAWP.2019.2919692.

[29] S. Liu, D. Yang, and J. Pan, "A low-profile broadband Dual-Circularly-Polarized metasurface antenna," *IEEE Antennas Wireless Propag. Lett.*, vol. 18, no. 7, pp. 1395–1399, Jul. 2019, doi: 10.1109/LAWP.2019.2917758.

[30] Y. Juan, W. Yang, and W. Che, "Miniaturized low-profile circularly polarized metasurface antenna using capacitive loading," *IEEE Trans. Antennas Propag.*, vol. 67, no. 5, pp. 3527–3532, May 2019, doi: 10.1109/TAP.2019.2902735.

[31] C. Zhao and C.-F. Wang, "Characteristic mode design of wide band circularly polarized patch antenna consisting of H-Shaped unit cells," *IEEE Access*, vol. 6, pp. 25292–25299, 2018, doi: 10.1109/ACCESS.2018.2828878.

[32] F. H. Lin and Z. N. Chen, "Low-profile wideband metasurface antennas using characteristic mode analysis," *IEEE Trans. Antennas Propag.*, vol. 65, no. 4, pp. 1706–1713, Apr. 2017, doi: 10.1109/TAP.2017.2671036.

[33] W. E. I. Liu, Z. N. Chen, and X. Qing, "Miniature wideband non-uniform metasurface antenna using equivalent circuit model," *IEEE Trans. Antennas Propag.*, vol. 68, no. 7, pp. 5652–5657, Jul. 2020, doi: 10.1109/TAP.2019.2957971.

[34] R. Martens, E. Safin, and D. Manteuffel, "Inductive and capacitive excitation of the characteristic modes of small terminals," in *Proc. Loughborough Antennas Propag. Conf.*, Loughborough, U.K., Nov. 2011, pp. 1–4. Accessed: May 04, 2015. [Online]. Available: http://ieeexplore.ieee.org/xpls/abs_all.jsp?arnumber=6114141

[35] E. Newman, "Small antenna location synthesis using characteristic modes," *IEEE Trans. Antennas Propag.*, vol. 27, no. 4, pp. 530–531, Jul. 1979, doi: 10.1109/TAP.1979.1142116.

[36] M. Cabedo-Fabres, E. Antonino-Daviu, A. Valero-Nogueira, and M. Bataller, "The theory of characteristic modes revisited: A contribution to the design of antennas for modern applications," *IEEE Antennas Propag. Mag.*, vol. 49, no. 5, pp. 52–68, Oct. 2007.

[37] *FEKO–EM Simulation Software*. Accessed: Sep. 27, 2020. [Online]. Available: http://www.feko.info

[38] E. Safin and D. Manteuffel, "Reconstruction of the characteristic modes on an antenna based on the radiated far field," *IEEE Trans. Antennas Propag.*, vol. 61, no. 6, pp. 2964–2971, Jun. 2013, doi: 10.1109/TAP.2013.2251312.

[39] Z. Wu, L. Li, Y. Li, and X. Chen, "Metasurface superstrate antenna with wideband circular polarization for satellite communication application," *IEEE Antennas Wireless Propag. Lett.*, vol. 15, pp. 374–377, 2016, doi: 10.1109/LAWP.2015.2446505.

[40] A. Bhattacharyya, O. Fordham, and Y. Liu, "Analysis of stripline-fed slot-coupled patch antennas with vias for parallel-plate mode suppression," *IEEE Trans. Antennas Propag.*, vol. 46, no. 4, pp. 538–545, Apr. 1998, doi: 10.1109/8.664118.

[41] N. Nasimuddin, Z. N. Chen, and X. Qing, "Bandwidth enhancement of a single-feed circularly polarized antenna using a metasurface: metamaterial-based wideband CP rectangular microstrip antenna.," *IEEE Antennas Propag. Mag.*, vol. 58, no. 2, pp. 39–46, Apr. 2016, doi: 10.1109/MAP.2016.2520257.

[42] J. A. Sheersha, N. Nasimuddin, and A. Alphones, "A high gain wideband circularly polarized antenna with asymmetric metasurface," *Int. J. RF Microw. Comput.-Aided Eng.*, vol. 29, no. 7, Jul. 2019, Art. no. e21740, doi: 10.1002/mmce.21740.

[43] H. Li, S. Sun, W. Li, M. Wu, and C. Zhou, "Systematic pattern synthesis for single antennas using characteristic mode analysis," *IEEE Trans. Antennas Propag.*, vol. 68, no. 7, pp. 5199–5208, Jul. 2020, doi: 10.1109/TAP.2020.2978939.

FRANCESCO ALESSIO DICANDIA (Member, IEEE) was born in Carrara, Italy, in 1988. He received the bachelor's and master's degrees in telecommunications engineering and the Ph.D. degree in information engineering from the University of Pisa, Pisa, Italy, in 2012, 2014, and 2018, respectively. His research interests include reconfigurable antennas, characteristic modes analysis, multiple-input and multiple-output antennas, non-Foster matching networks, and chipless RFID sensors.

SIMONE GENOVESI (Senior Member, IEEE) received the Laurea degree in telecommunication engineering and the Ph.D. degree in information engineering from the University of Pisa, Pisa, Italy, in 2003 and 2007, respectively. Since 2003, he has been collaborating with the Electromagnetic Communication Laboratory, Pennsylvania State University (Penn State), University Park. From 2004 to 2006, he has been a Research Associate with the ISTI Institute of the National Research Council of Italy (ISTI-CNR), Pisa. From 2015 to 2017, he was several times a short-term Visiting Researcher with the Grenoble Institute of Technology, Valence, France, and University Rovira I Virgili, Tarragona, Spain. He is currently an Associate Professor with the Dipartimento di Ingegneria dell'Informazione, University of Pisa. He is the Coordinator of the Additive Manufacturing founded in the framework of the Departments of Excellence (Dipartimenti di Eccellenza) funded by the Italian Ministry of Education, University, and Research. His research interests include radio frequency identification (RFID) systems, reconfigurable antennas, and metamaterials.

• • •